Draft version February 7, 2022
Typeset using LaTeX **preprint** style in AASTeX631

Stellar Mass-to-light Ratios: Composite Bulge+Disk Models and the Baryonic Tully-Fisher Relation

James Schombert,[1] Stacy McGaugh,[2] and Federico Lelli[3]

[1]*Institute of Fundamental Physics, University of Oregon, Eugene, OR 97403*
[2]*Department of Astronomy, Case Western Reserve University, Cleveland, OH 44106*
[3]*Arcetri Astrophysical Observatory (INAF), Florence, Tuscany, IT*

ABSTRACT

We present stellar population models to calculate the mass-to-light ratio (Υ_*) based on galaxy's colors ranging from *GALEX* FUV to *Spitzer* IRAC1 at 3.6μm. We present a new composite bulge+disk Υ_* model that considers the varying contribution from bulges and disks based on their optical and near-IR colors. Using these colors, we build plausible star formation histories and chemical enrichment scenarios based on the star formation rate-stellar mass and mass-metallicity correlations for star-forming galaxies. The most accurate prescription is to use the actual colors for the bulge and disk components to constrain Υ_*; however, a reasonable bulge+disk model plus total color only introduces 5% more uncertainty. Full bulge+disk Υ_* prescriptions applied to the baryonic TF relation improves the linearity of the correlation, increases the slope and reduces the total scatter by 4%.

1. INTRODUCTION

The stellar mass of a galaxy is one of its most fundamental characteristics because it incorporates the end-point of baryon mass evolution (from atomic and molecular gas into stars and stellar remnants). Surprisingly, the path to understanding dark matter is to first understand stellar populations in galaxies. For example, the total baryonic mass of galaxies (gas and stars) tightly correlates with the "flat" circular velocity, which is driven by the dark matter halo in the standard cosmological context (McGaugh *et al.* 2000; Verheijen 2001; Lelli *et al.* 2019). The properties of such baryonic Tully-Fisher relation (bTF) unavoidably depend on the way we measure gas and stellar masses (e.g., Lelli *et al.* 2016). The gas component has relatively small uncertainties of the order of 10%: the gas mass is given by HI observations of atomic hydrogen plus minor statistical corrections for heavier elements and molecules (see McGaugh, Lelli, Schombert 2020). This leaves the stellar mass as the remaining unknown to the total baryonic mass, where the stellar mass can be deduced from the galaxy's luminosity with an assumed mass-to-light ratio (Υ_*) deduced from stellar population models, or by kinematic determinations of the mass surface density after subtracting the gas component (Martinsson *et al.* 2013).

The determination of stellar mass also has two components, one observational (photometry), the other computational (stellar population models to deduce Υ_*). Galaxy photometry, from the UV to the far-IR, has improved to the point where uncertainties in galaxy luminosity are driven by the definition of which galaxy components one wishes to examine rather than photometry errors (see Stone *et al.* 2021). While different galaxy types entail different challenges in our photometry methods, the uncertainties are well-known and less of a challenge to estimate.

The last remaining step is the application of Υ_* to the galaxy luminosity and this involves several paths. First is the specification of the correct Υ_* to apply to a particular part of a galaxy, or to the galaxy as a whole. Second, outlining the numerous details that go into the calculation of Υ_*, i.e. the star formation and chemical history of the portion of the galaxy to be converted into a stellar population model and, then, into stellar mass (Ge *et al.* 2021). Third, isolating the inherent uncertainties due the possible variations in the stellar tracks and chemical enrichment scenarios and how they reflect into the uncertainties on the final stellar mass (Lower *et al.* 2020). The goal of this paper is to provide the community with a straight-forward procedure to calculate the stellar mass of a galaxy using spatial color information to guide the stellar population models and evolution scenarios. We divide galaxies into their bulge and disk components, although the models are sufficient to calculate a total stellar mass simply from the galaxy's morphological type plus total luminosity.

Throughout this paper, we test our stellar population models using two galaxy samples with multiband photometry from the far ultraviolet (UV) to the near infrared (IR). The SPARC sample consists of 175 spiral and dwarf galaxies with high-quality HI rotation curves; the photometry is described in Lelli *et al.* (2016) for the Spitzer 3.6 μm band and in Schombert *et al.* (2019) for the other bands. The S^{4}G sample consists of 790 galaxies in common between the S^{4}G survey (Sheth *et al.* 2010) and the SDSS survey (Blanton *et al.* 2017); the multiband photometry was re-done by our team to measure accurate colors within the same physical aperture (see Schombert *et al.* 2019) and to distinguish bulge and disk components (this paper).

2. STELLAR POPULATION MODELS

The core to any stellar mass project are SSP (single/simple stellar populations) models produced by several groups over the past decade (see Conroy & Gunn 2010). SSPs are single burst models that start with a fiducial stellar distribution given by an assumed initial mass function (IMF) at a set metallicity, then ages them with standard stellar evolutionary tracks. One can then use these SSPs to produce a population of stars formed in a series of single burst events, where the length of the burst is short enough to ignore the small spread in age. During a short burst, the chemical evolution is also negligible so the metallicity of all of the stars are identical and unchanging per timestep. Thus, a complicated star formation history for a galaxy can be represented by a series of SSPs of varying ages and metallicity to match an assumed star formation rate (SFR) as a function of time plus a chemical evolution scenario. At any particular timestep, the observables can be extracted, such as a integrated spectra or color.

There are numerous variables that can enter into the construction of a SSP (see Ge *et al.* 2019). For example, one can introduce dust or emission lines. The IMF can be varied. Or the evolution of AGB (asymptotic giant branch) stars can be altered to simulate variations owing to metallicity changes. The number of blue main sequence stars or blue stragglers can be varied to represent star formation (SF) by strong cloud collision events that are richer in high mass stars. Turbulence can be introduced to increase the stellar rotation factors in stellar evolutionary tracks. These effects, and other nuances, were investigated in Schombert, McGaugh & Lelli (2019, hereafter SML) and make particular predictions to the run of color vs color for galaxies, reflecting into our uncertainty in Υ_* (see §6).

In addition, real galaxies do not form all of their stars in an instantaneous burst like an SSP, even massive ellipticals that have initial star forming events that last only over a few Gyrs (Thomas *et al.* 2005). Thus, a star formation history (SFH) is assumed, a distribution of star formation rate (SFR) with time. The assumption of a smooth SFR allows for the SFH to be broken down into a series of bins of unique age that matches an individual SSP, and a metallicity per bin that can be varied to match an assumed chemical evolution model. Each bin in time is weighted by the number of stars (formed during that timestep and normalized to the total

mass of the galaxy), and summed with all the older stars to produce a total color/spectra as a function of time.

The goal of exploring the use of stellar population models is that, if some of the characteristics of the chemical evolution and SFH of a galaxy is known, then one can deduce a unique set of colors that, in turn, result in a unique value of Υ_* deduced from the models. In other words, SFH plus metallicity maps into color that, in turn, results into a unique model value of Υ_* with some, hopefully, limited range of uncertainty.

An addition complication (and opportunity) is presented by the process of galaxy formation where, frequently, a rotating galaxy is clearly composed of two distinct stellar components, a bulge and disk (Sandage & Tammann 1983). Just based on their observational differences (bulges are redder and have spectral signatures of older stars, Tasca & White 2011), two different SFHs and chemical enrichment schemes should be applied to each region resulting in different Υ_* values. These values are then applied separately to the distinct luminosities that represent the populations in the disk and bulge. Some knowledge of the galaxy type and structure then allows those two components to be added in a luminosity-weighted fashion to produce a total color and total Υ_*. Our ultimate goal, then, is to present a simple empirical method of relating galaxy color to Υ_*, whether this be a disk or bulge or a user defined combination of the two, with clearly defined uncertainties to that value.

3. MAPPING THE STAR FORMATION HISTORY OF GALAXIES

In general, we can divide the star formation histories in galaxies into two simplistic models that map into the simple morphological division of early-type versus late-type galaxies (see Peterkin *et al.* 2021). The first scenario is an early, strong burst with rapid chemical enrichment and a sharp decline in the star formation after the burst (shown in Figure 1). This produces a present-day population that is primarily old and metal-rich, a common feature of ellipticals, S0s and bulges. A second scenario is given by a slowly declining or constant SFR plus a steady chemical enrichment process proportional to the SFR. While simplistic, this scenario matches most of the characteristics of early-type spirals, with red disks dominated by old stars, and late-type galaxies (Sc to Irr), rich in young, low metallicity stars (see discussion in §4 of SML).

The separation of bulges and disks, in terms of stellar populations, is similar to the division between ellipticals and spirals. The similarities between ellipticals, S0s and bulges has its origins in the earliest papers on galaxy photometry (Sandage & Visvanathan 1978). With the inclusion of S0s (as nearly non-star-forming disk galaxies), one finds a subset of galaxies with old ages (τ >10 Gyrs) and high metallicities ($Z > 2Z_\odot$). Bulges and ellipticals have similar structure, being $r^{1/4}$ in shape, which is normally associated with the process of a rapid conversion of gas into stars (MacArthur *et al.* 2008). For our work, we will continue to assume this simple version of the SFH for bulges, varying only the final metallicities to explain the range in bulge color (Tonini *et al.* 2016, Calura & Menci 2011).

One of the key diagnostics to unravel the SFH in star-forming disks is the so-called main-sequence of star-forming galaxies, a correlation of stellar mass and current SFR (see Speagle *et al.* 2014 and references therein). As discussed in McGaugh, Schombert & Lelli (2017), the main-sequence of galaxies displays a distinct break at $M_* = 10^{10} M_\odot$ where higher mass spirals display the traditional exponentially declining SFH after an early strong initial burst (Speagle *et al.* 2014). This explains their high stellar masses with a high current SFR, but red disk colors (a great deal of past SF leaving a numerically larger old, red population in the disk). Below $10^{10} M_\odot$ we find the realm of low mass disks and dwarfs that must have nearly constant SF over a Hubble time to explain their current SFR and stellar masses (McGaugh *et al.* 2017). While there is some flexibility in the SFH of high mass spirals, their colors rule out a number of more extreme SFHs (see discussion in SML). Low mass disks have very little flexibility in their past SF, for even their current SF

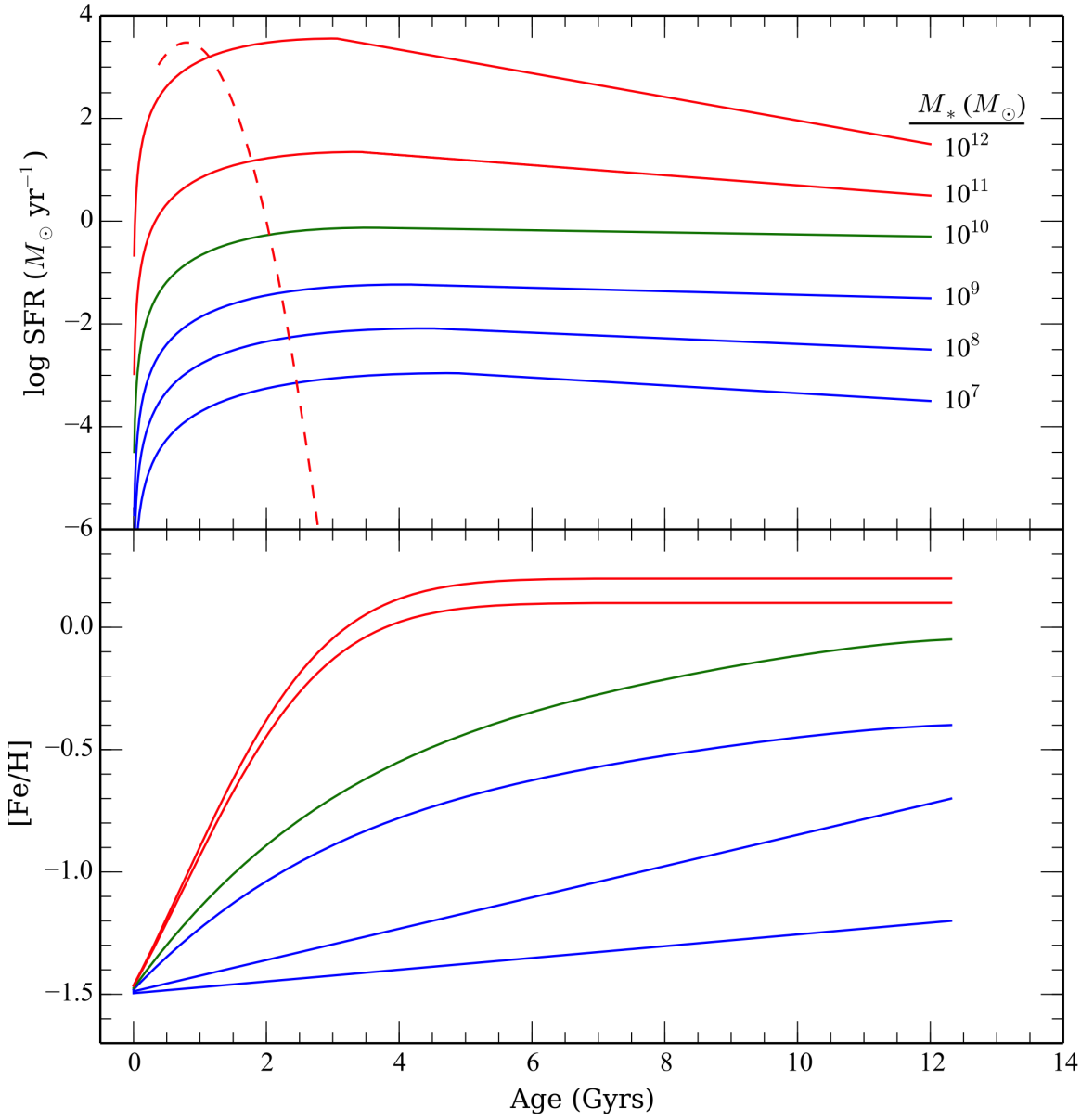

Figure 1. Baseline star formation and chemical enrichment histories as a function of stellar mass. The red curves are for high-mass ($M_* > 10^{10} M_\odot$) spiral galaxies that follow the Speagle *et al.* $z = 0$ main-sequence. The blue curves are adjusted to match the low-mass main-sequence found by McGaugh, Schombert & Lelli (2017) with near constant SF over a Hubble time. The green line is an intermediate, canonical SFH for a Milky Way sized system. The early, strong SF for the high mass galaxies results in the formation of red disks for early-type spirals. The low intensity, constant SF in low mass galaxies results in low density (i.e., LSB), low metallicity stellar populations. A 10 Gyrs burst model for a 10^{12} $M_\odot$ bulge is shown as the red dashed line. The bottom panel displays the adopted chemical enrichment scenarios for the SFH in the upper panel. The final metallicity is set by the mass-metallicity relation for star-forming galaxies (Cresci *et al.* 2018). Bulges are assumed to have very fast enrichment to present-day values, thus, no chemical evolution history is presented in the bottom panel.

barely creates enough stellar mass over a Hubble time and are fixed with a nearly constant SF scenario with some room for an early epoch of burst SF so as to form bulges or pseudo-bulges. Their low metallicities from emission line measurements (plus color-magnitude diagrams) also eliminates scenarios with strong bursts of SF separated by long quiescent phases (Schombert & McGaugh 2021).

The deduced baseline SFHs are shown in Figure 1 for final stellar masses of 10^7 to $10^{12} M_\odot$ (see SML for a more detailed discussion). While a majority of the stellar mass in disk galaxies is in the disk, the increase in bulge mass can be seen reflected in the higher SFRs at early epochs for the high mass spirals. Other styles of SFH are considered, such as later initial formation times, but, again, the more extreme scenarios can be rejected based on the comparison between observed and predicted optical to near-IR colors. These colors represent various slices of time in the SFH (for example, UV colors represent stars of only a few hundred Myrs) and measure any sharp changes from the current SFR over time scales of Myrs to Gyrs (again, see SML for a fuller discussion, particularly Figure 2 of that paper).

Likewise the chemical history of high and low mass disks are similarly constrained by the correlation between stellar mass and current mean metallicity (Weldon *et al.* 2020). The mass-metallicity relation, while having different slopes for disk and bulges (Cresci *et al.* 2018, Li *et al.* 2018), still defines a monotonic increase in mean galaxy metallicity with stellar mass. This reflects the obvious correlation that more SF results in more stellar mass while at the same time resulting in more element recycling and, therefore, increasing chemical enrichment (see Prantzos & Boissier 2000). The greatest unknown here is the rate of chemical enrichment with time, which reflects into the ratio of metal-poor to metal-rich stars per generation.

The strength of the initial SF epoch, combined with the known rapid chemical enrichment phenomenon for strong bursts (Maiolino & Mannucci 2019), results in a proposed slow versus fast enrichment models (see bottom panel of Figure 1). Slow in the sense that low mass dwarf galaxies begin with initial populations having mean [Fe/H] values between -2 and -1.5 but only reach current values of -0.7 to -0.5 (in agreement with their very low SFRs averaged over a Hubble time). This process must proceed in proportion to the SFR, thus the expectation of more metal-poor stars per generation than a galaxy with faster enrichment (i.e., higher average SFR resulted in more stellar mass, Gavazzi *et al.* 2002). Over the same timescale, high mass disks proceed from similar starting values to reach super-solar values in their star-forming regions and the metal-rich bulge within a few Gyrs after initial SF (i.e., fast). Quantitatively, this results in more low metallicity old populations (i.e., bluer) in low mass galaxies versus more metal-rich (i.e., redder) in high mass disks for the same age. This is the primary reason that LSB galaxies have bluer colors compared to similar mass HSB galaxies (Schombert & McGaugh 2015), although the difference is negligible for this study.

Since past SFH defines the final stellar mass, which in turn determines the final mean metallicity, the interrelated nature of the SF process allows the construction of a fairly constrained set of galaxy color/spectra models from the deduced SFH and a simple chemical enrichment model. The sum of a finite set of SSPs of a specific age and metallicity (at that age) produces a unique present-day galaxy spectra from which we can extract characteristics, such as color and Υ_*. The adopted, baseline evolutionary scheme is shown graphically in Figure **??** where the final SFR, metallicity and stellar mass are used to set the zeropoint for each model. Low mass galaxies have current SFR versus total stellar masses slighter richer than a pure constant SFR model, so some early SF is assumed, which is in agreement HST imaging of nearby LSB dwarfs (Schombert & McGaugh 2021). The presence of a significant $r^{1/4}$ bulge in higher mass disks results in a model with a canonical strong initial burst followed by an exponential decline as outlined by Speagle

et al. (2014). The primary consistency check for these models is an accurate reproduction of the various two-color diagrams (e.g, optical to near-IR colors as shown in Figure 6 of Schombert & McGaugh 2014).

In our previous paper (SML), the models had difficulty reaching very red and very blue colors. On the red side, this is due to the problem that any recent SF dominates the optical colors (pushing them blueward) even at very low levels typical of Sa and S0 galaxies (Yildiz *et al.* 2017). The reason may be threefold: (1) the increasing contribution of a large bulge in early-type spirals, (2) increasing reddening from the dust component (Schombert *et al.* 2013), and (3) possible shutdown of the star-formation at least 1 Gyrs ago in Sa/S0s (Johnston *et al.* 2014). On the blue side, the assumption of a constant SFR means that at very low levels of SFR (log SFR < -4) luminosity from the star-forming component is very weak (even in an LSB disk) and metallicity effects dominate the colors. In fact, it was impossible to produce $B-V$ colors less than 0.4 or $V-[3.6]$ colors less than 2.0 using these assumptions (extremely blue colors are primarily the domain of bright starburst galaxies).

In order to extend the SF models to redder and bluer colors we have made two addition assumptions. On the red side, we assume that redder colors are primarily in higher mass spirals with past histories of high SFR (building large and old disks). Rather than attempting to model the complex process of star formation quenching in red disks, or an increased dust contribution, we have simply extrapolated models with $V-[3.6]$ colors of 3.1 to 3.3 ($B-V$ from 0.8 to 0.9) in a linear fashion to cover the reddest disks. The resulting models produce red disk colors owing to an increasing fraction of old, intermediate to high metallicity stars, rather than a change in their SF histories. With respect to integrated total colors, the reddest spirals also have large bulges that begin to dominate their colors for type Sa/Sb galaxies. This does not seem to be an unreasonable extension to the models but we indicate this extension with a dashed line in Figure 2.

The blue side is more problematic. The bluest galaxies divide into two classes; 1) LSB dwarfs with very low SFRs and very low metallicities (Schombert & McGaugh 2015) versus 2) starburst dwarfs, such as blue compact dwarfs (BCDs, McQuinn *et al.* 2010, Gil de Paz & Madore 2005) with high current SFRs relative to their stellar mass. The LSB dwarfs are nearly within our model colors for the lowest current, and past, SFR. But the models fail to reach $B-V$ colors less than 0.45, nor $V-[3.6]$ colors bluer than 2.0, which describes about 10% of the S^4G survey (Sheth *et al.* 2010). These bluer galaxies (both LSB and HSB in nature) indicate our assumption of declining or nearly constant SF is violated in the last 500 Myrs (the last slice of time that effects both optical and near-IR colors).

To explore the low mass galaxies with bluer colors, we relax the constant SF constraint for the last 500 Myrs and study three scenarios; 1) a decrease from the past SFR by 50%, 2) an increase from the past SFR by 10% and 3) and increase from the past SFR by 50%. These three scenarios were not chosen arbitrary but rather were guided by our previous discovery of a variation of the low mass end of the main-sequence with respect to far-UV colors (see SML and Cook *et al.* 2014). As noted in SML, there is a distinct division on galaxies with blue versus red *GALEX* FUV-NUV colors (see Figure 1 of SML). Galaxies with FUV-NUV colors less than 0.25 lie above the constant SFR line, those with redder colors lie below. This indicates a slight change in the most recent SFR compared to the average SFR in the past. Numerical experiments focused on far-UV colors, which range from 0.0 to 0.6 for low mass galaxies in the Cook *et al.* 2014 and SPARC samples (Schombert & McGaugh 2014, see inset histogram of Figure 2). The decreasing SF scenario results in FUV-NUV colors around 0.5, a weak increase produces colors near 0.3 and a strong burst results in FUV-NUV near zero. These models result in $V-[3.6]$ colors between 2.0 and 2.5 (depending on final metallicity) and recover the bottom portion of the two color diagrams (see §4 and Figure 2).

We can also distinguish between very blue LSB dwarfs and starburst systems by morphology and central surface brightness. Typically, these very blue galaxies correlate in morphology with their far-UV colors: the blue FUV-NUV galaxies (with FUV-NUV < 0.25) are high in surface brightness with Irr or IB type morphologies (none earlier than Sc, Cook *et al.* 2014). Whereas, redder near-UV colors are found in LSB disks and dwarfs with blue near-IR colors from low metallicities ($V - [3.6] < 2.0$), but not the sharp optical $B - V$ colors ($B - V < 0.4$) seen in starburst BCDs. We present both endpoints, with respect to Υ_*, in the following discussions. In that respect, we find that most LSB dwarfs follow an extrapolation of our SFH models to the lowest metallicities that have slightly rising Υ_* values. However, this is balanced by the fact that even a single O star complex in a very low surface density environment drives Υ_* downward. A system with constant SF for 10 Gyrs, with a halt in SF for the last Gyr, has an Υ_* of 0.5 at 3.6μm. We use this as the bottom limit for our models, but caution the reader that very blue starburst galaxies will have lower Υ_* by a factor of 2 to 3 (see §4).

4. TWO COLOR DIAGRAMS

As a reality check, we require some observables other than those used to generate the SFH model (i.e., SFR and mean [Fe/H]) to compare with model predictions. Galaxy colors can serve that role, particularly by comparison of widely separated colors in wavelength space to capture the subtle effects from different types of stars; such as blue main sequence (bMS), AGB and RGB stars. The two colors of choice for this comparison are $B-V$ and $V-[3.6]$ as they are influenced by very different ages in a typical stellar population and display different sensitivities to metallicity effects. The optical color ($B - V$) primarily follows changes owing to recent SF (the dominance of O to A stars). The near-IR color ($V - [3.6]$) covers the region dominated by RGB and AGB stars (the strength of the old population plus metallicity from the position of the RGB). There is a still a degree of degeneracy in using just two colors (see Schombert & McGaugh 2014 for a fuller discussion); however, for our purposes of confirming a level of accuracy to our star formation models, this two color diagram serves as a sufficient standard. Those two colors are shown in Figure 2 of SML for 790 galaxies in a combined S^4G and SPARC sample selected for accurate ground-based and *Spitzer* photometry (see SML for details of the extracted photometry).

The photometry used are total colors derived from curves of growth to SDSS and *Spitzer* images. Thus, bulge and disk components are summed in this diagram, although one can see the effect of an increasing red bulge component for early-type spirals. The curvature in this diagram signals a number of known stellar population changes. For example, galaxies with the bluest $V - [3.6]$ colors have the bluest $B - V$ colors, but reach a plateau in $B-V$ around 0.45 for $V-[3.6] < 2.7$. This is due to the fact that $V-[3.6]$ quickly reddens with only a small increase in $B - V$ signaling the first onset of very red, yet young, AGB stars a few Gyrs after the initial SF events. At redder $B - V$ colors, the increasing bulge component drives the $B - V$ values steadily to the red for early-type spirals, but the $V - [3.6]$ near-IR color barely changes owing to a steady contribution from AGB stars and the fact that metallicity changes very little for early-type disks (a flattening of the mass-metallicity relation at high stellar masses). The large spread in colors is probably a indicator that this process is not as smooth as our baseline models assume where the actual process of SF proceeds in a series of small bursts (a “flicker" SFH, see McQuinn *et al.* 2010). These bursts then average in color space due to the large timesteps needed to produce detectable changes in broadband colors. Fortunately, the exact process of SF is irrelevant to the calculation of Υ_* as long as the process is monotonic on timescales of Gyrs.

The division by galaxy type (RC3 T-type, Buta *et al.* 1994) is also evident in Figure 2 of SML, although the overlap in both colors is considerable. Since bulge-to-disk (B/D) ratio also correlates with galaxy type

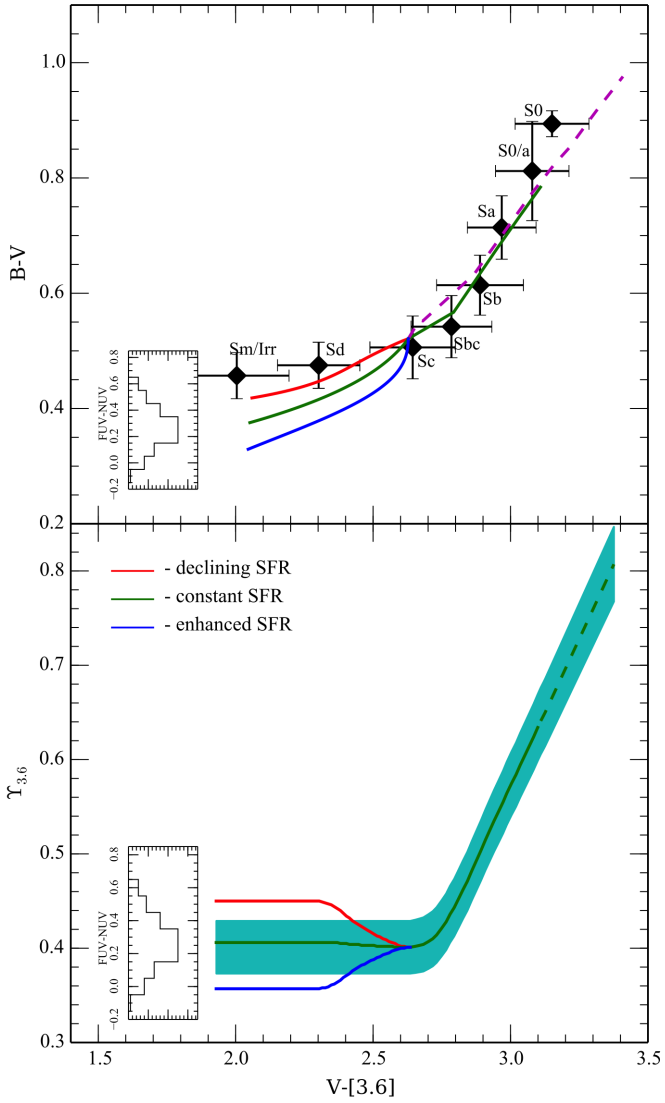

Figure 2. The top panel displays the average optical to near-IR colors for the SPARC and S^{4}G samples by galaxy type. The errorbars display the 3σ dispersion of the averages (not error in the colors). The green track is the baseline SFH model from SML (2019). The dashed line is the new bulge+disk model that captures the redder colors of early-type spirals (see §5). Three burst models are shown for late-type galaxies; red for a declining SFR, green for a constant SFR and blue for a weak increase in recent SFR. A inset histogram of UV colors displays the observed FUV-NUV colors matching the endpoint of each late-type model (where the mean FUV-NUV color matches the constant SF model). The bottom panel displays the effect of those same models on the deduced mass-to-light ratios. Here the solid lines represent the original models adjusted on the blue side for late bursts of SF and extrapolated on the red side (dashed line) to capture older and more metal-rich red disks. Some knowledge of the optical color or morphology of a blue galaxy can reduce the uncertainty in Υ_* by 15% on the blue end. The cyan band indicates the range in uncertainty in Υ_* owing to scatter in the mass-metallicity and main-sequence relations.

(Graham & Worley 2008), we can use the model colors outlined in §3 to map each model onto a unique B/D to calculate the relative weight of the bulge and disk components. Operationally, we use the average $B-V$ and $V-[3.6]$ colors for each galaxy T-type in the S^{4}G and SPARC samples (using NED to extract the RC3 morphologies) and define a mean B/D per color. The average colors for each T-type are shown in Figure 2

using their standard Hubble designations. It was found that galaxy T-types 1 and 2 had identical colors, thus they are summed to form type 1.5 (basically all Sa galaxies). Likewise, types 6 and 7 were similar (late-type Sc) and were averaged to 6.5. Everything later than Sd were degenerate in their optical colors, so 8, 9 and 10 were summed into type 9 (basically a bin of all Sm/Irr types). The errorbars are 3σ dispersions, not uncertainties on the colors.

The nominal baseline model colors from SML are shown as the green track in Figure 2 and does a fair job of matching the colors for galaxy types from Sa to Sc. The models do not reach the bluest near-IR colors for the galaxy types later than Sd, which is probably due to deviations from the constant SF assumption in low stellar density environments. An extrapolation of the low metallicity models using the scenarios discussed in §3 results in the red and blue tracks in Figure 2. These two tracks simulate a slight rise or decline in the current SFR that drive optical and near-IR colors on timescales less than 0.1 Gyrs. This type of behavior is also evident in CMDs for star-bursting dwarfs from Weisz *et al.* (2011).

To extend the SFH models to redder colors, we need to deduce the effect of the bulge colors on the total colors displayed in Figure 2. The SPARC sample provides a unique view of the interior color distribution because over one half the sample has both *Spitzer* and SDSS imaging, plus another quarter of the sample have UBV values from the RC3. Full imaging allows for the separation of the bulge and disk components, and a direct comparison of the colors of those components can guide the construction of our bulge+disk color models. The SPARC sample has a full range of galaxy types, central surface brightness, morphology and luminosities so selection effects are minimized.

For our analysis, we define a break point in the 3.6 surface brightness profile where the bulge dominates over the disk. Interior to that radius, an elliptical aperture (defined again by the 3.6 isophotes) is applied to each SDSS g and *Spitzer* 3.6 frame. These luminosities are subtracted to deduce a bulge color. The corresponding disk color is deduced by subtracting the bulge luminosity from the total luminosity of the galaxy (based on curves of growth). Experiments with varying break radii finds that the bulge and disk colors are stable to the 2% level, typically owing to the fact that bulge surface brightnesses are much higher than disk surface brightnesses, but the bulge area is smaller than the disk area.

There are solid correlations between bulge/disk colors and the total luminosity of a galaxy such that brighter spirals have redder colors (Kennedy *et al.* 2016). These are mostly dominated by the correlation between stellar mass and metallicity (where luminosity is a proxy for stellar mass and color is a proxy for mean metallicity), but is somewhat surprising as there is no particular dominant scenario where bulge and disk formation are synchronised (although, clearly, larger initial gas mass will lead to larger bulges and larger disks which drives the final color). In addition, as the main-sequence relation indicates that all spirals below $10^{10} M_{\odot}$ have nearly constant SF for a Hubble time, they all also have the roughly the same distribution of stellar ages in their stellar population (Weisz *et al.* 2011). Therefore, the correlation with color appears to be driven by chemical enrichment rather than age although a sharper decline in SF for high mass spirals will result in more older (and redder) stars.

The difference between the bulge-luminosity and disk-luminosity correlations are notable. As expected, bulges are redder than disks at any particular bulge luminosity; however, the difference in colors is roughly constant with disk color. Bulges are, on average, 0.3 mags redder than disks in $V - [3.6]$, although on a case-by-case basis there is a great deal of variation. The distinction is sharper for classic $r^{1/4}$ shaped bulges versus disks; decreasing in difference for pseudobulges whose low luminosities distort the separation of bulge and disk light.

We can use this fact to constrain the disk+bulge models in §5, where for a given total color, there is a unique disk and bulge color combination that matches the expected B/D ratio of that total color (since color correlates with morphology). In other words, for each disk model that produces a disk color X, there is a bulge model of color $X + 0.3$ that serves as the bulge population color. We can consider the scatter in the bulge/disk color relation as the uncertainty in B/D ratios for purpose of evaluating a particular model.

5. BULGE+DISK MODELS

The SFH models outlined in the previous section are best applied to colors in regions of a galaxy with common SF and chemical enrichment scenarios. There is strong observational evidence that bulge and disk components have very different kinematic and SF histories (van den Bosch 1998). In particular, the different structural shapes plus opposite optical to near-IR colors signals different evolutionary paths. The most significant difference is, of course, the distinct lack of current SF in bulges compared to the fact that ongoing SF dominates the appearance of disks. Thus, it seems inappropriate to use the same models for star-forming disks to deduce Υ_* in bulge regions.

The best scenario to model bulges is the well-established single burst model used so successfully to predict the colors of ellipticals (see Samland & Gerhard 2003). Under this approximation, the bulges are assumed to be single burst population of singular age with a metallicity that is proportional to their total mass (see Schombert & Rakos 2009). For our study, we have adopted an age of 10 Gyrs and a range of final metallicities from [Fe/H] = −1.0 to +0.2 (see Costantin *et al.* 2021). This metallicity distribution covers the range in optical and near-IR colors displayed by bulges in the SPARC sample on the assumption that metallicity is the primary driver of bulge color.

While there is not a perfect correlation between bulge and disk color, we can use the trend in disk to bulge color to select a bulge color (and, thus, a unique model) based on the disk color and model. With our baseline scenario, we assume a mean difference of 0.3 mags in $V - [3.6]$ color from the disk to the bulge. Thus, when we blend the disk and bulge components (for an assumed B/D ratio), we can use a bulge model that matches the disk color (increased by 0.3 mags). In general, these bulge colors represent a slightly higher metallicity than the disk model, but one would expect the bulge metallicity to be slightly higher than the final disk metallicity due to a more rapid onset of chemical enrichment from the bulge's initial burst of SF as well as expected reservoirs of low metallicity gas available to disk.

Lastly, there is the assignment of the B/D ratio for the summed bulge and disk components. The B/D ratio is primarily a function of galaxy type (although, operationally, it is galaxy type that is dependent on the visual B/D for types Sa to Sc). Galaxy type is also strongly correlated with galaxy color (Graham & Worley 2008). Therefore, we can use model color to assign a galaxy type and, thereby, a B/D ratio. A small amount of iteration is required, as we start with a pure disk color, then extract a mean B/D ratio followed by the application of the luminosity ratio using a bulge color from the bulge versus disk color diagram.

To summarize, models of star-forming disks are produced using a grid of population models of ages and metallicities given by the mean SFHs taken from the main-sequence relationship (normalized by stellar mass, outlined in SML) and the mass-metallicity relation, as shown in Figure 1. The near-IR disk colors are calculated from the model, then used to assign a galaxy type by color (near-IR colors are used as they are less sensitive to sharp changes in the recent SFR). From the galaxy T-type, a B/D is assigned based on the grid of B/D and morphological type (Graham & Worley 2008). A 10 Gyrs burst bulge model is calculated and summed with the disk colors to deduce a total near-IR color. This value will typically underestimate the correct B/D as the disk colors will always be bluer than the bulge colors for the first estimate. A short iteration is made of the disk and bulge models to match the total $V - [3.6]$ color to the correct B/D ratio,

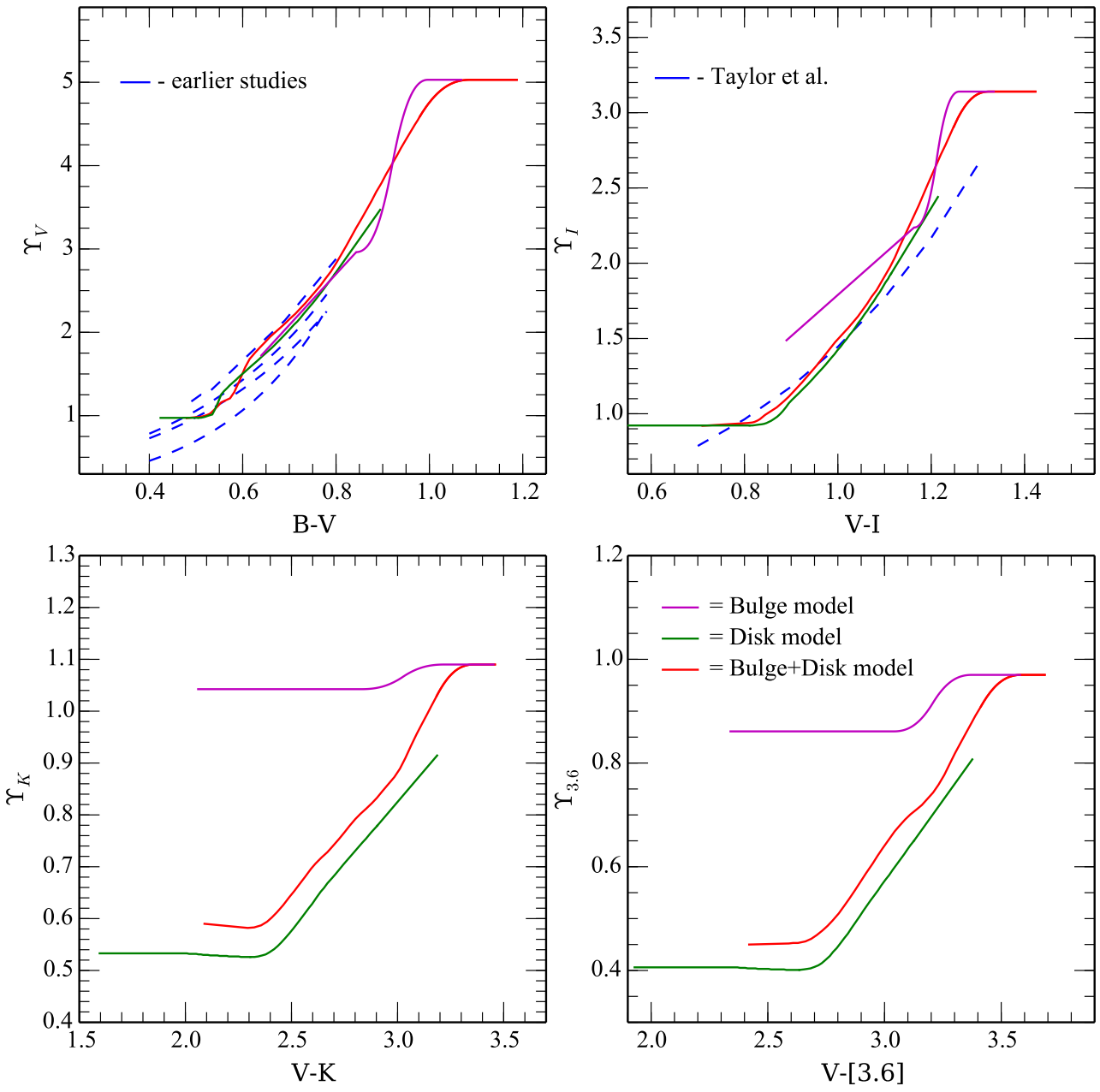

Figure 3. Four Υ_* models for the optical and near-IR (V, I, K and IRAC 3.6). The green lines are the SFH models from SML (extended to redder and bluer colors as discussed in text). A 10 Gyr bulge model is shown as a purple line in each panel. The merged bulge+disk models are shown in red. As the models progress from the near-IR to the optical, the difference between the various models merge as the youngest stars dominate in the optical. The slope of the color-Υ_* relation steepens with bluer filter, meaning that errors in optical colors will reflect into larger Υ_* errors compared to the near-IR. Also shown in the $B-V$ panel are previous color-Υ_* studies discussed in Schombert & McGaugh (2014, blue dashed lines) and in the $V-I$ panel the relationship defined by Taylor *et al.* (2011) for SDSS i photometry. Bulge+disk models are needed to extend these older studies to redder colors, but agrees well with our newer models. The Taylor *et al.* relation is in agreement with intermediate colors, but deviates significantly for red, early-type galaxies.

then the resulting model is converted into colors from optical to near-IR. Note, those same models have unique Υ_* values for the disk and bulge components, which are summed (weighted by near-IR luminosity) for a total Υ_* for each model color.

The track of total color ($B-V$ versus $V-[3.6]$) for these bulge+disk models is shown in Figure 2. At the bluest colors, the contribution from the bulge is negligible and the colors converge to the baseline disk SFH models. As the bulge light increases in fractional contribution, we see the colors moving redward compared to the baseline models. Again, the sharp rise in near-IR color ($V-[3.6]$) for the bluest galaxies signals the first epoch of AGB stars entering the near-IR bandpasses. Both the baseline and bulge+disk models are slightly bluer then the average optical color of late-type galaxies, perhaps due to an underestimate of the AGB component (Schombert & McGaugh 2015). As the models approach the reddest galaxies, the bulge contribution dominates and approaches the red region representing the colors of ellipticals (Schombert 2016). Solar metallicity models match the reddest spirals, but the models overestimate the near-IR colors for non-star-forming E/S0s, again probably due to mismatch of the AGB contribution for old populations plus an underestimate of the contribution from a hot component such as old, low metallicity, blue horizontal branch (BHB) stars (see Schombert & Rakos 2009). An increase in mean metallicity by 0.2 dex on the AGB component brings the Sb to Sc values in agreement with the colors. The effect of these changes on Υ_* is discussed in §6; however, in general, the predicted colors are in good agreement with the observed colors of the S^{4}G and SPARC samples.

Matching the blue disk models to the bulge+disk models (blueward of $V-[3.6]=2.6$) requires an estimate of the style of SF in the last 500 Myrs. Our three scenarios, matched to far-UV colors, are shown in the top panel of Figure 2 for the two color diagram and in the bottom panel for their effect on the correlation between color and Υ_*. Our original declining SF model predicts a slight rise in Υ_* below $V-[3.6]=2.6$. However, the constant SF model predicts a constant Υ_* below $V-[3.6]=2.6$ and the increasing SF model predicts a slightly lower Υ_*. The range in Υ_* at 3.6μm is from 0.35 to 0.45. A mean of 0.5 has been used in past studies (see Lelli *et al.* 2016). But better UV or near-blue color information can reduce the uncertainties by 15% (we note that FUV-NUV or $B-V$ or a morphology estimate are all equally effective at defining Υ_* on the blue side).

The ultimate goal of the SFH models is, of course, the extraction of a Υ_* for each model (i.e., each galaxy color). These values are filter dependent, and we express their values as a function of the color V-X, where X is the filter of interest. Four examples are shown in Figure 3 for filters B, I, K and IRAC 3.6. The blue curves are the same as those from SML, extrapolated now to the cover the reddest and bluest galaxies in the SPARC dataset. The bulge model is constant in Υ_* in the near-IR until metallicities rise high enough for a decrease in the AGB population luminosity and sequential rise in Υ_*. The bulge+disk model have slightly higher Υ_* values at all points, representing the higher Υ_* from the bulge population, and merge with the disk and bulge models at the bluest and reddest colors. The extrapolated disk model is for LSB dwarfs on the main-sequence diagram and with very low metallicities using the constant SF model from Figure 2.

In general, one finds that Υ_* increases steadily with redder colors (a higher percentage of older stars with high Υ_* values). Also, the slope of the color versus Υ_* relation becomes shallower with increasing wavelength (and the dynamic range is reduced). Aside from lower extinction effects owing to dust, this is the primary reason that near-IR photometry produces superior Υ_* estimates. As one goes to optical filters, small errors in galaxy color produce larger errors in Υ_* compared to near-IR filters. This same trend is found by numerous previous studies. For example, also shown in the $B-V$ panel of Figure 3 are the results from four previous studies on Υ_* in the optical (Portinari *et al.* 2004, Zibetti *et al.* 2009, Into & Portinari

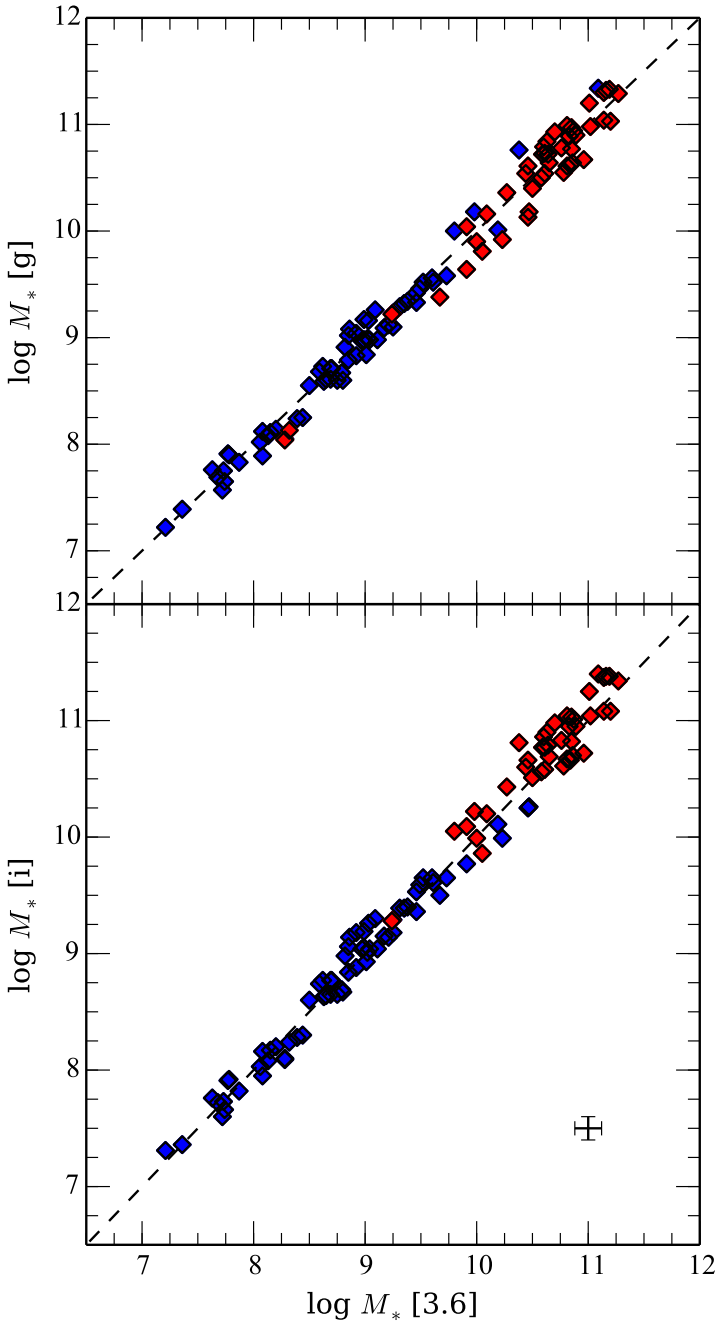

Figure 4. A comparison of deduced stellar masses using SDSS g, i and *Spitzer* 3.6 photometry plus the new bulge+disk models from Figure 3. The SPARC sample is divided into red and blue galaxies based on colors greater or less than $g - i = 1.05$ or $V - [3.6] = 2.9$. The agreement across various optical and near-IR filters is excellent with no obvious systematics. The dispersion increases slightly to bluer filters in expectation with the increase in color versus Υ_* slopes for bluer colors.

2013, and Roediger & Courteau 2015, see also SML). Although they all use varying assumptions on the

SFH of star-forming galaxies, the slopes are remarkable similar and the mean, at any particular $B-V$ value, is similar to both our SF and bulge+disk models. A webtool to compute Υ_* is available for the community[1].

A different technique was presented by Taylor *et al.* (2011) using a sophisticated Bayesian parameter fitting to the optical SED from SDSS photometry. They present a SDSS $g-i$ vs Υ_* relation and an analytic fit arguing that the use of UV and near-IR colors only marginally improves the accuracy of estimating Υ_* from SDSS i photometry. Their $g-i$ relationship is shown in the $V-I$ panel (green dashed line) and is an excellent match for intermediate colors, but underestimates Υ_* for the redder colors compared to our bulge+disk model. This difference is primarily due to our empirical treatment of the AGB contribution, particularly in near-IR filters. While their analysis of the deficiencies in the near-IR differs from our conclusions, we note that the dynamic range in the *Spitzer* bandpasses is a factor of six less than in the SDSS i filter, with a corresponding decrease in uncertainty. In addition, their $g-i$ estimator severely underestimates the Υ_* values for early-type spirals and ellipticals, which can have a significant impact on the results from lensing studies that late-type and early-type galaxies differ in their positions on the radial acceleration relation (see Brouwer *et al.* 2021).

As a consistency test, we compare the stellar masses for the SPARC sample deduced from the bulge+disk models using SDSS g, SDSS i and *Spitzer* IRAC 3.6 images in Figure 4. The only sources of error in this comparison are the errors in the photometry (both absolute and in color) and the uncertainties in the parameters that went into the bulge+disk models. While there is a wide range of metallicities and ages that correspond to a particular color (and, thus, a value for Υ_*), the main-sequence and mass-metallicity relations appear to constrain the range in models enough to produce an excellent agreement between the deduced Υ_* values from the near-blue to the near-IR. There are no obvious systematics by mass or galaxy color. The dispersion is higher than the expected error based solely on the photometry, this would indicate that the scatter in color reflects real scatter in the age and metallicity of the underlying stellar population and the use of the Υ_* models is limited by knowledge of the stellar characteristics beyond the mass-metallicity and main-sequence relations.

6. UNCERTAINTIES IN DEDUCING Υ_*

The key to our analysis of Υ_* is the fact that a unique SFH and metallicity distribution for a composite stellar population maps into a unique SED (i.e., color) and, therefore, a unique Υ_*. The uncertainty in Υ_*, then, has three components; 1) errors in the galaxy photometry, 2) errors in the SSP SEDs and 3) variation in the main-sequence and mass-metallicity relations (as they reflect into the deduced stellar population model). First, we consider errors in the galaxy photometry. These arises not in an error of the total luminosity (which is to be converted into a total stellar mass), but rather into an error in the color used to deduce Υ_* from the bulge+disk models. An error in color magnifies as one goes to bluer filters, for the slope of the color versus Υ_* curve steepens. A typical magnitude error of 0.01 in luminosity, and 0.02 in color, corresponds to an uncertainty of 10% in Υ_* at V, but only 4% at 3.6μm. This is a strong argument for continuing to use near-IR bandpasses to measure stellar mass as the shallower Υ_*-color slope minimizes the effect of photometric error. We constrain the models using the mean colors per galaxy type, but assign the Υ_* values based on the individual galaxy colors that, in the end, results in an near equal contribution to the error budget. The errors in the galaxy photometry are well-known and discussed in the various photometry papers (see SML). The mean error varies slightly with galaxy type, but an error of 0.05 describes the entire sample within 20%.

The errors in the actual construction of the SSPs is quite small as the newest stellar libraries are highly detailed. The largest uncertainty in a composite SSP is how independent exotic components, such AGB or

[1] http://abyss.uoregon.edu/~js/sfh

BHB stars, are included. While the main sequence and RGB stars are fairly well-defined by the metallicity and age of the stellar population, the contribution from AGB stars can vary between various studies (see Eftekhari, Vazdekis & La Barbera 2021). We are guided, again, by the two color diagrams to constrain the more extreme models discussed in SML. While models with enhanced blue main sequence stars or suppressed AGB populations can explain the edges of the two color distribution of galaxies, they are frequently inconsistent with the mean colors of each galaxy type (see Figure 2). And the dispersion in color, per galaxy type bin, is consistent with the dispersion solely in metallicity and star formation history (see below). Thus, we adopt a typical error in the photometry as it maps into a range of the baseline models. For the SPARC and S^{4}G samples, the mean error in $V-[3.6]$ color is 0.05, that resolves into a model uncertainty in the near-IR of $\Delta\Upsilon_* = 0.04$.

Lastly, are the uncertainties introduced by a range in SFR and metallicity enrichment. An estimate of their effect on the models can be obtained by considering the scatter in the main-sequence and mass-metallicity relations as they reflect into the models. The main-sequence relation has two legs, the high mass end with a relatively shallow slope and the low mass end with a slope of near unity implying constant SF over a Hubble time. The SFH of low mass galaxies is highly constrained due to the limited time to produce their current stellar masses at their current SFRs. The UV color correlation within the main-sequence (Schombert, McGaugh & Lelli 2019) plus numerous resolved CMDs for nearby dwarfs, indicates that a series of micro-bursts (i.e., SF flickering, see McQuinn *et al.* 2010) rather than strictly constant SF will satisfy the lower main-sequence; however, each micro-burst is sufficiently low in intensity that it produces a composite stellar population that differs very little in mean colors from a constant SF model (except for the bluest UV colors). The high mass end of the main sequence contains galaxies with much higher current SFRs, but variations from the Speagle *et al.* models result, primarily, in early production of bulge stars and the resulting Hubble sequence of early-type spirals. Numerical experiments using the observed scatter in the main-sequence, mapped into models with varying SFR values, displays a dispersion in $V-[3.6]$ color of 0.04 on the blue end to 0.06 on the red side. This results in a dispersion of 0.02 to 0.06 in Υ_* for SFH effects.

The uncertainty in metallicity is deduced from the scatter in the mass-metallicity relation (see Kewley & Ellison 2008). Although slightly higher at lower metallicities, due to the low number of dwarfs in their sample, the mean dispersion is approximately 0.12 dex in [Fe/H] for the range in stellar masses considered by our study. Again, with numerical experimentation, this maps into a range of Υ_* between 0.02 and 0.05. Thus, the resulting uncertainty from the SFH and metallicity model inputs, if added in quadrature, are approximately 0.04 on the blue, low mass end and 0.06 on the red, high mass end. We note that this also maps into dispersions in color of 0.15 to 0.25 for $V-[3.6]$ which nicely brackets the observed dispersion in colors for the SPARC and S^{4}G samples. We conclude that most of the dispersion in galaxy color is, then, due to variations in SFH and chemical enrichment with respect to our baseline models. The dominant source of error in Υ_* is the range in possible SFH and metallicity that matches a particular galaxy color.

In summary, the uncertainty in Υ_* from photometric errors varies considerable with wavelength being minimal in the near-IR, although Figure 4 demonstrates that optical filters can achieve the same level of accuracy as near-IR filters with good colors. For highly accurate galaxy luminosities, the current limit in $\Delta\Upsilon_*$ has its origin in the dispersion in possible SFHs and internal metallicity distributions. This value is approximately 0.06 at 3.6μm (0.05 dex in log M_*). The uncertainty increases slightly on the blue and red ends of the color versus Υ_* relationship due to sharp, recent star formation events on the blue end, and the

effects of dust and metallicity on the red end. This is shown, graphically, in Figure 2 as the shaded band around the star-forming disk model.

7. CONVERSION FROM LUMINOSITY TO STELLAR MASS

Armed with these new models there are now four methods to convert galaxy luminosities into stellar masses by photometric means. We will demonstrate that our technique using Υ_* values deduced from *Spitzer* 3.6μm images for these luminosities has the narrowest range in Υ_* and the smallest scatter. The four methods are as follows; first, the application of a mean Υ_* value to the bulge and disk luminosities. This was the technique used in the earliest SPARC papers (Lelli *et al.* 2016) where an Υ_* of 0.5 was assumed for disks (the mean value from the pure disk models) and a value of 0.7 was assumed for the bulge component. The second method is to deduce a more accurate Υ_* value using the color information of each component. Thus, a Υ_* value for the disk is taken from the disk model and the color of the disk region. Likewise, a bulge Υ_* is deduced from the bulge color. These two values are then used to the observed disk and bulge luminosities and summed. The third method is used if only a total aperture color is available. Then, the total Υ_* is deduced from the total color and the bulge+disk models in Figure 3. This method will be the most useful for large galaxy surveys where the spatial information is not saved and only total colors and luminosities are extracted from the datasets. Lastly, if there is no color information, only a 3.6μm flux, then one can estimate the total Υ_* value from the galaxy morphology. Since morphology is correlated with color, one can go from estimated color to Υ_* with the bulge+disk model. There is an expectation that the second method is the most accurate as it uses all of the color information of a galaxy in a spatial way, with the third method producing similar values, statistically. The last method, by galaxy type, should be the least reliable and we can compare all our techniques to the original prescription from Lelli *et al.* (2016).

To test the different methods, we have plotted the calculated stellar masses for the SPARC dataset in Figure 5. Of the 175 galaxies in the SPARC dataset, 132 have SDSS imaging available from the DR16 archive. Another 22 have Johnson V aperture values available from NED. Of the 132 with SDSS imaging, 50 have classic $r^{1/4}$ bulges, 41 have pseudo-bulges (defined as a central concentration of light, but without a power-law profile) and 41 are pure disk systems based on examination of their surface brightness profiles (each type displayed as a different symbol color in Figure 5).

As can be seen in Figure 5, the late-type galaxies display very little change between the four methods. The primary offset is due to the change in the baseline disk model from a declining SFH to a constant SFH, which results in a shift from 0.50 used in the original SPARC sample, to a mean value of 0.41. Other than this constant shift, the disk model varies very little with color between $V - [3.6] = 1.5$ and 3.0 (where 90% of the disk colors lie). The early-type spirals display more scatter, again due to the nature of a color relationship where blue bulges have lower Υ_* values from the canonical value of 0.7 and red bulges have higher values. It is worth noting that using galaxy type as a proxy for color recovers a great deal of the estimated stellar mass compared to the canonical values, but consistently over estimates the mass value compared to color models.

An independent check on stellar mass-to-light ratios is provided by the velocity dispersions of face-on galaxies (e.g, Bershady *et al.* 2010, Martinsson *et al.* 2013). These appear to be in tension with stellar population models (Angus *et al.* 2016), but this seems to be caused by a difference in the populations tracing the stellar mass and those dominating the velocity ellipsoid traced by the available spectral lines (Aniyan *et al.* 2021). For the case of NGC 6946, our photometric estimate of the stellar surface density is in excellent agreement with that inferred kinematically by Aniyan *et al.* (2021).

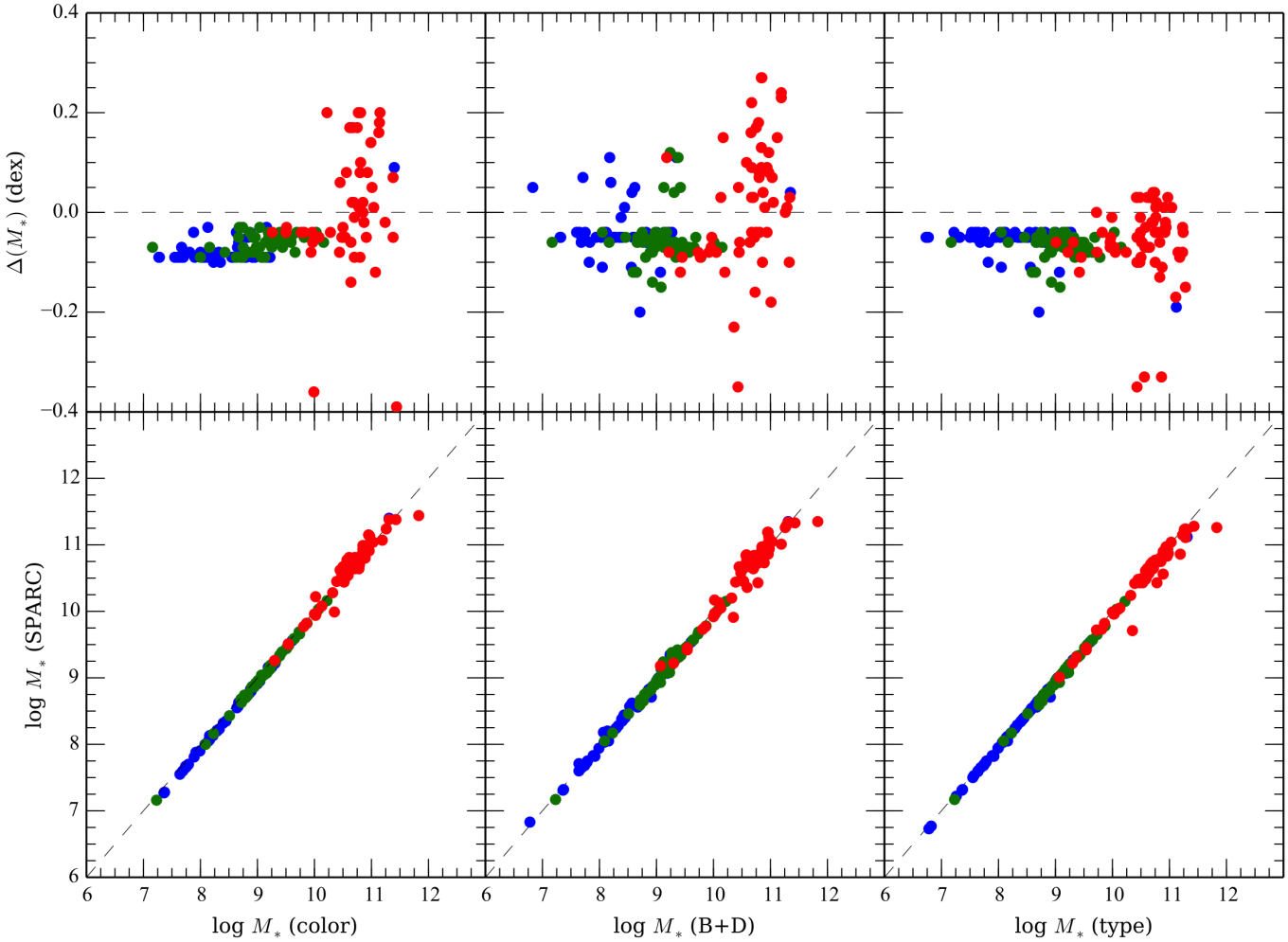

Figure 5. A comparison of the original Υ_* prescription (SPARC, Lelli *et al.* 2016) on the y-axis versus the three new color methods. The first panel uses the color of the separate disk and bulge components to derive Υ_* (using 3.6 luminosities). The second panel uses the combined B+D model and total galaxy color. The third panel uses the galaxy type to predict the total color, then applies the B+D model. The upper panels display the difference from unity in log space. Note the disk model assumes a new SFH of constant SFH for very blue galaxies (see Figure 2) with a mean Υ_* of 0.41 versus the assumed value of 0.5 in our previous papers. Red symbols galaxies with classic, $r^{1/4}$ bulges, green for pseudo-bulges and blue for pure disk systems. The most significant difference is the higher stellar masses for early-type spirals with the correct inclusion of bulges.

8. EFFECTS OF THE BTF RELATIONSHIP

The primary impact of new Υ_* models is their effect on the deduced stellar masses for baryon mass to kinematic relationships, such as the baryonic Tully-Fisher relation (bTF). The effect of the new models on the bTF can be seen in Figure 6. The original bTF for the SPARC sample uses distances from the EDD database (Tully *et al.* 2016) and velocities from Lelli *et al.* (2019). A full description of the dataset can be found at Schombert, McGaugh & Lelli (2020). The original bTF, used an Υ_* of 0.5 for disks and 0.7 for bulges and is shown in the upper left panel. The upper right displays the same relation using the actual color information of the disk and bulge. The lower left panel displays the application of B+D model to the total

color of the galaxy. And, lastly, the bottom right panel uses the relationship between galaxy morphological type and color to deduce Υ_* from the B+D model.

There are two points to note. First, the downward trend at high baryonic masses is significantly reduced with the color models where early-type spirals have higher stellar masses due to more accurate Υ_* from their disk and bulge colors. As high baryonic mass galaxies typically have low gas fractions, this change in Υ_* is more critical to their final baryonic mass values than for the low mass, high gas fraction galaxies. This upward adjustment of early-type spirals (basically due to the inclusion of an accurate bulge component) in the bTF supports the observation that the bTF is surprisingly linear in log space with a power-law slope of 4, in contrast to predictions from a ΛCDM cosmology (see also Di Teodoro *et al.* 2021).

Second, the scatter around the TRGB/Cepheid fit to the bTF (shown as the black line) is reduced by 5% for the color and B+D models. This is a promising trend for the bTF studies as a whole, but indicates diminishing returns even with more accurate colors. Point by point color analysis of the disks of spiral would be required, with more detailed modeling of the SFH of each point, in order to increase the accuracy of the Υ_* values and, therefore, the final stellar masses. Increasing the information of the interior stellar population, for example, by spectral indices, would improve the model fits and applied Υ_* values.

9. SUMMARY

We present a continuation of our color versus mass-to-light (Υ_*) studies of galaxies using stellar population models that include two important changes; 1) extensions to bluer and redder colors to match the observed range in real galaxies and 2) a new bulge+disk model to produce more accurate Υ_* for early-type spirals. While new stellar masses for late-type galaxies calculated from these new models differ very little from our original prescriptions, correct application of these models to the bulge and disk colors of early-type spirals can have factor of two change in their total stellar masses, which improves the linearity of the baryonic Tully-Fisher relation on the high mass end.

Our technique differs in several key ways from previous studies. To summarize:

- We deduce scenarios for the star formation history and chemical enrichment for galaxies using the main-sequence and mass-metallicity relations. Constrained by optical and near-IR colors, the baseline models predict the Υ_* across all filters of interest. The scatter in the main-sequence and mass-metallicity relations matches the dispersion in colors and provides a measure of uncertainty to the Υ_* versus color relations.

- We develop a series of different methods to calculate Υ_* using colors from different components (i.e., bulge and disk) versus total colors versus simple galaxy morphology, and confirm their internal consistency across multiple bandpasses. We confirm the accuracy of our SFH scenarios using the model predictions in two color space as well as galaxy morphology versus color diagrams. We find that UV and blue colors can reduce the uncertainty by 15% for low mass galaxies with irregular SFHs. A Υ_* webtool is available for the community at http://abyss.uoregon.edu/~js/sfh.

- We compare our new Υ_* values with our original SPARC stellar masses and find a negligible difference for low mass galaxies and a slight increase in the early-type spirals due to the proper treatment of a bulge component. The slight increase on the high mass end of the baryonic Tully-Fisher relation improves its linearity and reduces the error in the slope.

We found, in deference to other color versus Υ_* studies, that the near-IR filters produce the most accurate stellar masses and that further improvements to the accuracy of Υ_* will require more information of the SFH

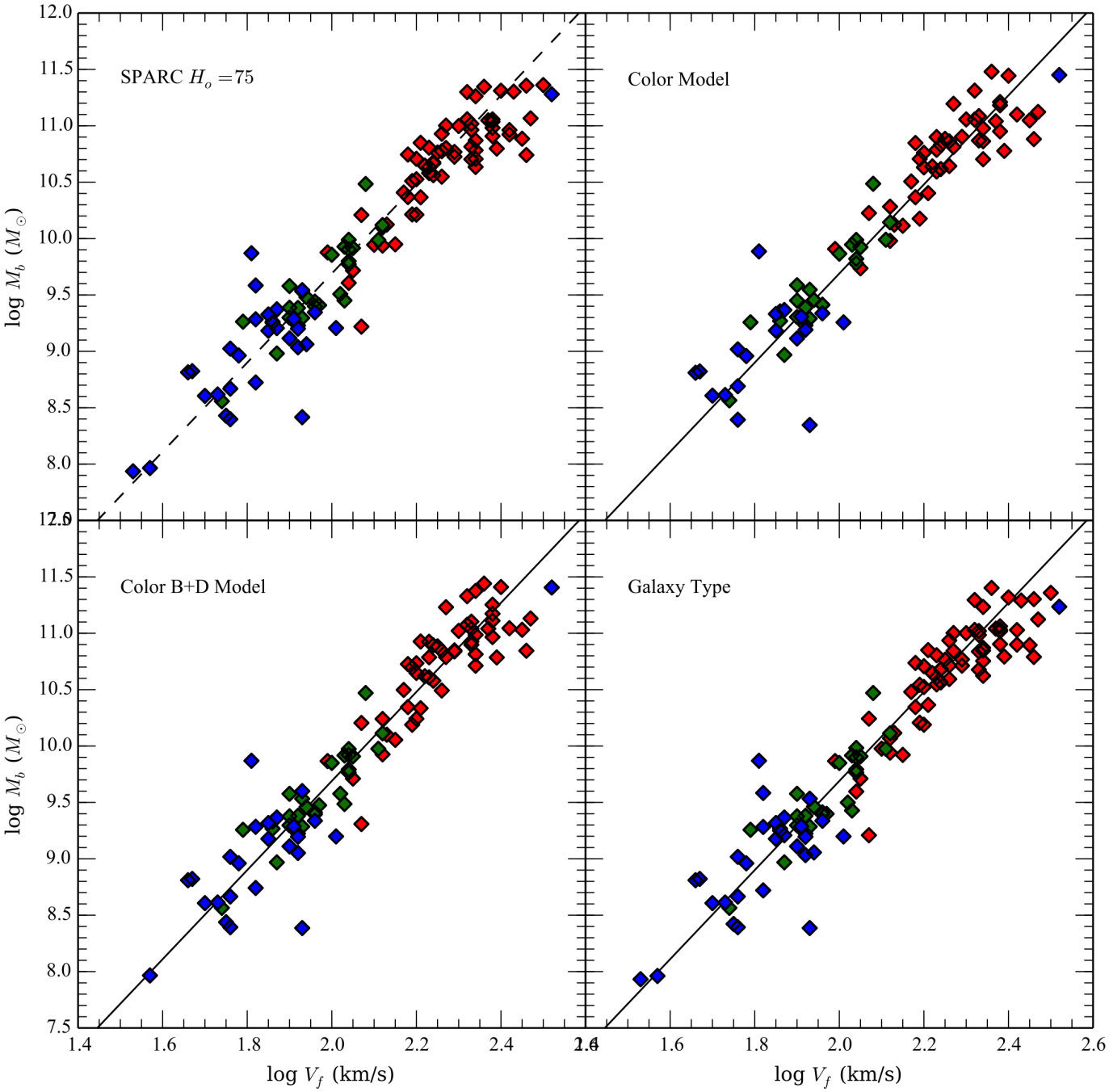

Figure 6. The changes in the baryonic Tully-Fisher relation using different Υ_* models. The upper left is the original SPARC dataset using EDD distances and flow models with H_o = 75. The upper right is the same kinematic data and distances, but calculating Υ_* from the colors of the bulge and disk components. Galaxies without spatial color information were left out of the sample. Bottom left is the two color B+D model and bottom right using only the galaxy type to set the galaxy color. Symbol colors are the same as Figure 5 for bulges, pseudo-bulges and pure disks. The bTF is significantly more linear with either color model, but scatter around the C/TRGB fit is only reduced by 5%.

of individual galaxies (e.g., through spectral indices). The uses of our new Υ_* models reduces the scatter in the baryonic Tully-Fisher relation. Analysis of the scatter in the baryonic Tully-Fisher relation suggests that there is no deviation from linearity in log space. Reducing scatter further in the bTF will require significant improvements to distance estimates rather than better galaxy photometry or kinematic work as the estimates of stellar masses are no longer the limiting parameter in the bTF.

Software for this project was developed under NASA's AIRS and ADP Programs. This work is based in part on observations made with the Spitzer Space Telescope, which is operated by the Jet Propulsion Laboratory, California Institute of Technology under a contract with NASA. Support for this work was provided by NASA through an award issued by JPL/Caltech. Other aspects of this work were supported in part by NASA ADAP grant NNX11AF89G and NSF grant AST 0908370. As usual, this research has made use of the NASA/IPAC Extragalactic Database (NED) which is operated by the Jet Propulsion Laboratory, California Institute of Technology, under contract with the National Aeronautics and Space Administration.

REFERENCES

Angus, G. W., Gentile, G., & Famaey, B. 2016, A&A, 585, A17. doi:10.1051/0004-6361/201527122

Aniyan, S., Ponomareva, A. A., Freeman, K. C., et al. 2021, MNRAS, 500, 3579.

Bershady, M. A., Verheijen, M. A. W., Swaters, R. A., et al. 2010, ApJ, 716, 198.

Blanton, M. R., Bershady, M. A., Abolfathi, B., et al. 2017, AJ, 154, 28. doi:10.3847/1538-3881/aa7567

Brouwer, M. M., Oman, K. A., Valentijn, E. A., et al. 2021, A&A, 650, A113. doi:10.1051/0004-6361/202040108

Buta, R., Mitra, S., de Vaucouleurs, G., et al. 1994, AJ, 107, 118. doi:10.1086/116838

Calura, F. & Menci, N. 2011, MNRAS, 413, L1. doi:10.1111/j.1745-3933.2011.01017.x

Conroy, C. & Gunn, J. E. 2010, ApJ, 712, 833. doi:10.1088/0004-637X/712/2/833

Cook, D. O., Dale, D. A., Johnson, B. D., et al. 2014, MNRAS, 445, 899

Costantin, L., Pérez-González, P. G., Méndez-Abreu, J., et al. 2021, ApJ, 913, 125. doi:10.3847/1538-4357/abef72

Cresci, G., Mannucci, F., & Curti, M. 2019, A&A, 627, A42. doi:10.1051/0004-6361/201834637

Di Teodoro, E. M., Posti, L., Ogle, P. M., et al. 2021, MNRAS, 507, 5820. doi:10.1093/mnras/stab2549

Eftekhari, E., Vazdekis, A., & La Barbera, F. 2021, MNRAS, 504, 2190. doi:10.1093/mnras/stab976

Ge, J., Mao, S., Lu, Y., et al. 2019, MNRAS, 485, 1675. doi:10.1093/mnras/stz418

Ge, J., Mao, S., Lu, Y., et al. 2021, MNRAS, 507, 2488. doi:10.1093/mnras/stab2341

Gil de Paz, A. & Madore, B. F. 2005, ApJS, 156, 345. doi:10.1086/427068

Graham, A. W. & Worley, C. C. 2008, MNRAS, 388, 1708. doi:10.1111/j.1365-2966.2008.13506.x

Gavazzi, G., Bonfanti, C., Sanvito, G., et al. 2002, ApJ, 576, 135.

Into, T. & Portinari, L. 2013, MNRAS, 430, 2715. doi:10.1093/mnras/stt071

Johnston, E. J., Aragón-Salamanca, A., & Merrifield, M. R. 2014, MNRAS, 441, 333. doi:10.1093/mnras/stu582

Kennedy, R., Bamford, S. P., Häußler, B., et al. 2016, A&A, 593, A84. doi:10.1051/0004-6361/201628715

Kewley, L. J. & Ellison, S. L. 2008, ApJ, 681, 1183. doi:10.1086/587500

Lelli, F., McGaugh, S. S., & Schombert, J. M. 2016, AJ, 152, 157. doi:10.3847/0004-6256/152/6/157

Lelli, F., McGaugh, S. S., Schombert, J. M., et al. 2019, MNRAS, 484, 3267.

Li, H., Mao, S., Cappellari, M., et al. 2018, MNRAS, 476, 1765. doi:10.1093/mnras/sty334

Lower, M. E., Bailes, M., Shannon, R. M., et al. 2020, MNRAS, 494, 228.

MacArthur, L. A., Ellis, R. S., Treu, T., et al. 2008, ApJ, 680, 70. doi:10.1086/587887

Maiolino, R. & Mannucci, F. 2019, A&A Rv, 27, 3. doi:10.1007/s00159-018-0112-2

Martinsson, T. P. K., Verheijen, M. A. W., Westfall, K. B., et al. 2013, A&A, 557, A131.

McGaugh, S. S., Schombert, J. M., & Lelli, F. 2017, ApJ, 851, 22. doi:10.3847/1538-4357/aa9790

McGaugh, S. S., Lelli, F., & Schombert, J. M. 2020, Research Notes of the American Astronomical Society, 4, 45.
McQuinn, K. B. W., Skillman, E. D., Cannon, J. M., et al. 2010, ApJ, 724, 49. doi:10.1088/0004-637X/724/1/49
Moster, B. P., Naab, T., & White, S. D. M. 2013, MNRAS, 428, 3121. doi:10.1093/mnras/sts261
Peterken, T., Aragón-Salamanca, A., Merrifield, M., et al. 2021, MNRAS, 502, 3128.
Portinari, L., Sommer-Larsen, J., & Tantalo, R. 2004, MNRAS, 347, 691. doi:10.1111/j.1365-2966.2004.07207.x
Prantzos, N. & Boissier, S. 2000, MNRAS, 313, 338.
Roediger, J. C. & Courteau, S. 2015, MNRAS, 452, 3209. doi:10.1093/mnras/stv1499
Samland, M. & Gerhard, O. E. 2003, A&A, 399, 961. doi:10.1051/0004-6361:20021842
Sandage, A. & Visvanathan, N. 1978, ApJ, 223, 707. doi:10.1086/156305
Sandage, A. & Tammann, G. A. 1983, Ciel et Terre, 99, 63
Schombert, J. & Rakos, K. 2009, AJ, 137, 528. doi:10.1088/0004-6256/137/1/528
Schombert, J., McGaugh, S., & Maciel, T. 2013, AJ, 146, 41. doi:10.1088/0004-6256/146/2/41
Schombert, J. & McGaugh, S. 2014, PASA, 31, e036. doi:10.1017/pasa.2014.32
Schombert, J. & McGaugh, S. 2015, AJ, 150, 72. doi:10.1088/0004-6256/150/3/72
Schombert, J. M. 2016, AJ, 152, 214. doi:10.3847/0004-6256/152/6/214
Schombert, J., McGaugh, S., & Lelli, F. 2019, MNRAS, 483, 1496. doi:10.1093/mnras/sty3223
Schombert, J., McGaugh, S., & Lelli, F. 2020, AJ, 160, 71. doi:10.3847/1538-3881/ab9d88
Schombert, J., McGaugh, S., & Lelli, F. 2020, AJ, 160, 71. doi:10.3847/1538-3881/ab9d88
Schombert, J. & McGaugh, S. 2021, AJ, 161, 91. doi:10.3847/1538-3881/abd54d
Sheth, K., Regan, M., Hinz, J. L., et al. 2010, PASP, 122, 1397
Speagle, J. S., Steinhardt, C. L., Capak, P. L., et al. 2014, ApJS, 214, 15. doi:10.1088/0067-0049/214/2/15
Stone, C. J., Arora, N., Courteau, S., et al. 2021, MNRAS, 508, 1870. doi:10.1093/mnras/stab2709
Tasca, L. A. M. & White, S. D. M. 2011, A&A, 530, A106.
Taylor, E. N., Hopkins, A. M., Baldry, I. K., et al. 2011, MNRAS, 418, 1587. doi:10.1111/j.1365-2966.2011.19536.x
Thomas, D., Maraston, C., Bender, R., et al. 2005, ApJ, 621, 673. doi:10.1086/426932
Tonini, C., Mutch, S. J., Croton, D. J., et al. 2016, MNRAS, 459, 4109. doi:10.1093/mnras/stw956
Tully, R. B., Courtois, H. M., & Sorce, J. G. 2016, AJ, 152, 50. doi:10.3847/0004-6256/152/2/50
Weisz, D. R., Dalcanton, J. J., Williams, B. F., et al. 2011, ApJ, 739, 5. doi:10.1088/0004-637X/739/1/5
Weldon, A., Ly, C., & Cooper, M. 2020, MNRAS, 491, 2254. doi:10.1093/mnras/stz3047
Zibetti, S., Charlot, S., & Rix, H.-W. 2009, MNRAS, 400, 1181. doi:10.1111/j.1365-2966.2009.15528.x
van den Bosch, F. C. 1998, ApJ, 507, 601. doi:10.1086/306354
Verheijen, M. A. W. 2001, ApJ, 563, 694.
Yıldız, M. K., Serra, P., Peletier, R. F., et al. 2017, MNRAS, 464, 329. doi:10.1093/mnras/stw2294